

Final Draft
of the original manuscript:

Deprez, E.; Justo, A.; Rojas, T.C.; Lopez-Cartes, C.; Bonatto Minella, C.;
Boesenberg, U.; Dornheim, M.; Bormann, R.; Fernandez, A.:
**Microstructural study of the LiBH₄–MgH₂ reactive hydride
composite with and without Ti-isopropoxide additive**
In: Acta Materialia (2010) Elsevier

DOI: 10.1016/j.actamat.2010.06.043

Microstructural study of the LiBH₄-MgH₂ reactive hydride composite with and without Ti-isopropoxide additive

E.Deprez, A.Justo, T.C.Rojas, C.López-Cartés, C.Bonatto Minella, U.Bösenberg, M. Dornheim, R.Bormann, A.Fernández

Abstract

An exhaustive microstructural characterization is reported for the LiBH₄-MgH₂ reactive hydride composite (RHC) system with and without the Ti-isopropoxide additive. X-ray diffraction (XRD) with Rietveld analysis, transmission electron microscopy (TEM) coupled to energy dispersive X-ray analysis (EDX), selected area electron diffraction (SAED) and electron energy loss spectroscopy (EELS) are presented in this paper as the first time for this system in all sorption steps. New data are reported regarding average crystallite and grain size, microstrain, phase formation and morphology that contribute to the understanding of the reaction mechanism and the influence of the additives on the kinetics. Microstructural effects, related to the high dispersion of titanium based additives, results in a distinct grain refinement of MgB₂ and an increase of reaction sites which causes acceleration of desorption and absorption reactions. Considerations on stability of phases under e-beam irradiation have been also reported.

Keywords

Hydrogen storage, Nanocomposite, Microstructure, X-ray diffraction, Transmission electron microscopy

Introduction

Hydrogen is one of the favoured energy carriers for the future since it has the highest energetic power, it is a non polluting fuel and energy and water are the only combustion products [1-3]. In addition to liquid and compressed gas storage, metal hydrides can store hydrogen safely and reversible at high volumetric densities. However, at present, no single metal hydride fulfils the requirements posed for mobile applications regarding both gravimetric density and suitable reaction enthalpies.

Lithium borohydride (LiBH₄) is a very interesting material because of its high theoretical gravimetric capacity (18.5 wt%) [4-5]; however, it still suffers from slow reaction kinetics and high thermodynamic stability. By formation of a composite with

MgH₂, MgB₂ is formed during desorption and thereby the overall reaction enthalpy is lowered. This allows for lower reaction temperatures while maintaining a high gravimetric storage capacity [6,7]. The dehydrogenation of 2LiBH₄+MgH₂ occurs according to the reaction: 2LiBH₄+MgH₂ ↔ 2LiH+MgB₂+4H₂ which releases about 10.5 wt% of hydrogen, additionally the reaction is found to be reversible at moderate conditions. The formation of MgB₂ appears to stabilize the dehydrogenated state and therefore decreases the total reaction enthalpy of the system. The pure LiBH₄ has been shown to be reversible [8-10] but at much higher temperature than the RHC.

Depending on pressure and temperature, the LiBH₄-MgH₂ reactive hydride composite (RHC) shows a two-step desorption mechanism. First, MgH₂ desorbs and forms Mg; thereafter LiBH₄ decomposes forming LiH and MgB₂ whereby more hydrogen is released [11, 12]. The appearance of an incubation period between the two steps described by Bösenberg et al. [11] makes the overall reaction very slow. However, the incubation period could be overcome and the kinetics could be enhanced by suitable additives, such as transition metal chlorides or oxides [11-14]. Particularly, the metal organic compound titanium isopropoxide (Ti-iso) has shown to significantly improve the kinetics of the 2LiBH₄-MgH₂ system and especially the desorption of LiBH₄ [11].

Previous work on the chemical state of transition-metal-based additives indicated the formation of transition-metal borides during synthesis or cycling [15-18]. Very recently a TEM study [19] has demonstrated the formation of small additive nanoparticles in the grain boundaries upon cycling for the case of Zr-based additives. Several factors, related to favouring heterogeneous nucleation of MgB₂ and the increase of reaction sites through grain refinement have been proposed as potential origins for the observed kinetic improvement [15-19].

Characterization of the additives in the initial and cycled composites was a first step towards understanding the function and mechanism of the additives [18]. In this work an exhaustive microstructural characterization is reported for the 2LiBH₄-MgH₂ RHC system with and without the Ti-iso additive. XRD with Rietveld analysis, TEM studies coupled to EDX, SAED and EELS are presented here as the first time for this system in all sorption steps. New data are reported regarding average crystallite and grain size, microstrain, phase formation, stability under electron-beam irradiation and morphology that contribute to the understanding of the reaction mechanism and the influence of the additives on the kinetics.

Experimental

Sample preparation

The initial microcrystalline powders, LiBH_4 (95% purity), MgH_2 (98% purity, the rest being Mg) and Titanium isopropoxide (99.995% purity) were purchased from Alfa Aesar. Samples were then prepared by high energy ball milling in a Spex 8000 mixer mill using a ball (steel) to powder ratio of 10:1. The MgH_2 was premilled for 5 hours before being mixed to LiBH_4 and 5 mol% of Ti-iso for a further 5 hours milling. A set of samples without additive was also prepared to be studied.

To prepare the samples after desorption and re-absorption, hydrogen cycling was performed using a thermovolumetric Sieverts apparatus designed by Hydro Quebec/HERA Hydrogen Storage System. Desorption reactions were performed at 400 °C under 5 bar hydrogen, whereas the absorption reactions were measured at 350 °C under 50 bar hydrogen. The volumetric measurements were simultaneously performed to obtain desorption and absorption kinetic measurements.

All samples were prepared and handled under continuously purified argon or nitrogen atmosphere in gloveboxes.

Sample characterization

TEM analysis was performed in a Philips CM200 microscope operating at 200 kV. The microscope is equipped with an Energy-Dispersive X-ray (EDX) detector and a parallel detection electron energy loss spectroscopy (EELS) spectrometer from Gatan (766-2 kV). The B $K\alpha$ X-ray emission is in the low limit of detection in energy of the EDX system. Main conclusions have been therefore obtained here from the EELS data. Samples were diluted into dried toluene inside the glove-box, dropped onto a carbon coated copper grid and introduced into the microscope. A vacuum gate valve allowed the sample to be isolated in a pre-chamber for complete evaporation of toluene prior to transfer for analysis.

XRD measurements were performed with a powder diffractometer Siemens D5000-D with a goniometer for transmission geometry and carried out with Cu- $K\alpha$ radiation. Data acquisition was performed for 2θ angle range of 20-90 degrees. The samples were sealed in a glass capillary inside the glovebox. This experimental procedure has been proved to be very valuable to avoid air exposure and deterioration of the sample during recording of data. In addition, the light atomic weight of the main components in these

samples makes measurements in transmission mode well suited to achieve good signal to background ratio.

Diffraction patterns analyses were carried out using the MAUD software [20-21] based on Rietveld method. Crystallite sizes $\langle d \rangle$ and microstrain $\langle \varepsilon^2 \rangle^{1/2}$ were obtained by refinement of the experimental data. Peak shape was assumed to be a pseudo-Voigt (pV) function with asymmetry. The background of each pattern was fitted by a polynomial function of degree four. The accordance factor (R_{wp}) between experimental data and fit is reported for each pattern.

Results

i) Kinetic measurements and samples description

Figure 1, shows volumetric measurements of the desorption and absorption reactions of the reactive hydride composite $2LiBH_4+MgH_2$ with and without a 5 mol% Ti-iso additive, after activation by high energy ball milling.

For the experimental desorption temperatures of 400 °C and 5 bar hydrogen, desorption reaction proceeds in two steps [11-12]:



Figure 1a shows the incubation period between the two desorption steps substantially reduced by the addition of the Ti-iso additive [11]. Figure 1a shows also the third desorption kinetic curve for $2LiBH_4+MgH_2+5mol\%$ Ti-iso sample. Kinetics appears to be stabilized during the first cycles although a loss in hydrogen storage capacity is produced due most probably to partial oxidation of the sample upon cycling.

In this work RHC composite samples will be characterized in three steps: i) as prepared by high energy ball milling, ii) after first desorption and iii) after first rehydrogenation (1 cycle sample). Comparison is done for samples prepared with and without 5 mol% Ti-isopropoxide additive. Some studies were also done in a sample cycled 3 times in the presence of additive.

ii) X-ray diffraction analysis (XRD)

X-ray diffraction analysis was first carried out to identify the evolution of the crystalline phases in the RHC samples. Figure 2 shows the XRD patterns of $2LiBH_4+MgH_2$ and $2LiBH_4+MgH_2+5mol\%$ Ti-iso after ball milling (a) and first desorption (b) with indication of the expected peaks for reference phases indexes in the upper part of the figure.

Main peaks corresponding to the β -MgH₂ and LiBH₄ phases can clearly be distinguished in both as milled materials. The presence of a small amount of γ -MgH₂, formed during ball milling, is also detected. The position of a possible magnesium oxide phase is shown in figure 2a. The signal for this phase appears negligible as expected for the already observed formation of a 4 nm amorphous surface oxidation layer in MgH₂ [22]. The diffraction patterns obtained for the sample milled with the additive present smaller intensity as compared with the sample without additive. The effect is just a consequence of the absorption of the heavier Ti atoms due to the fact that diffractograms are measured in transmission mode inside a capillary.

After first desorption LiH and MgB₂ phases are observed (see figure 1b). The presence of crystalline MgO phases is now confirmed especially for the sample with the Ti-iso additive (shoulders at 2 θ angles of 43 and 62.5). This indicates that the additive is a source of oxygen introduced in the samples. The heating treatment at 400 °C is favouring the crystallization of amorphous oxide phases.

The as milled RHC samples, with and without additive, are compared in figure 3 with the samples after one cycle (desorption and re-absorption). The presence of the additive is again producing a decrease in the intensity of transmitted X-rays. It is observed after cycling an increase in crystallinity of the detected LiBH₄ and MgH₂ phases with a reduction of the background of the diffraction pattern. In addition the peaks of MgH₂ appear significantly bigger and narrower than the peaks of LiBH₄. A quantitative analysis will be presented below. As already mentioned, peaks of magnesium oxide phases are always more clearly visible (peak at ca. 43) for the samples with additive.

No crystalline phases containing the Ti additive could be detected in our XRD data. This is in agreement with the high dispersion and low content of the additive and the nanocrystalline/amorphous character of the Ti based active phases [18]. Other techniques like X-ray absorption spectroscopy and X-ray photoelectron spectroscopy were used in a previous paper [18] to determine the chemical state and phase formation of the Ti additive.

In order to obtain quantitative information about crystallite size and microstrain, Rietveld refinement analysis of the diffraction patterns was undertaken. The simplest Scherrer analysis has been demonstrated to be only a first approximation and microstrain needs to be considered. Figure 4 shows the results of the Rietveld refinement for a representative sample. A summary of obtained data is presented in Table I and Figure 5. We are interested in the evolution of crystallite size and

microstrain of the different phases and in the comparison of data for samples with and without additives. In Figure 5 data are presented only for the majority phases.

According to data in Table I and Figure 5, the as received LiBH_4 and MgH_2 samples show crystallite sizes in the micrometer range. The premilling of the MgH_2 produces, as expected, a strong reduction of the crystallite size down to tens of nanometers and a strong increase in the microstrain. The milling of LiBH_4 with pre-milled MgH_2 (with and without the additive) also produces a reduction of the crystallite size for the LiBH_4 phase, down to few hundreds of nanometer, together with an increase in the microstrain. The presence of the additive during the milling process does not affect significantly the crystal size for both LiBH_4 and MgH_2 , although an important increase in the microstrain is observed. A good dispersion of the additive is expected after the ball milling activation.

After the first desorption the LiH and MgB_2 phases are formed. In this case an important decrease in crystallite size by a factor of two was observed for both phases in the presence of the Ti-iso additive. The microstrain is however not being affected significantly.

The absorption process after the first desorption leads to the one cycle samples. A strong increase in the average crystallite sizes for the hydrided phases has been observed, especially for the MgH_2 , as compared with the initially milled material. Comparing the one cycled samples, with and without additives, a moderate decrease in average crystallite size was observed for the LiBH_4 and MgH_2 phases in the presence of the additive.

A sample milled with Ti-iso has been studied after 3 cycles. A progressive refinement of the microstructure has been observed (see Table I). This is in agreement with the measured stabilization of the kinetics as demonstrated in Fig. 1a for desorption.

iii) Transmission electron microscopy and spectroscopic analysis (TEM, SAED, EDX, EELS)

Microstructural and chemical analysis has been undertaken by combining the TEM and SAED with the EDX and EELS analysis inside the transmission electron microscope.

Figure 6 corresponds to the study of $2\text{LiBH}_4+\text{MgH}_2$ after ball milling. From the analysis in many different regions of the sample it was possible to identify particles with a darker contrast in the size range of 0.1-1 μm . The representative EDX analysis in region A of figure 6 allowed us to identify these particles as MgH_2 . They are polycrystalline, as

stated by SAED, and evolve to Mg by electron irradiation [22]. The electron diffraction pattern also shows the presence of diffuse rings that can be attributed to MgO as oxidation product of Mg. Inside these large polycrystalline particles, smaller and well defined nanocrystals could be detected by high resolution TEM [22], in good agreement with the average crystallite size of 12.6 nm determined for the β -MgH₂ phase by XRD. The de-hydrogenation of the MgH₂ particles by electron beam irradiation can also be detected by the EELS analysis in the low loss region (see Fig.6, EELS in region A). Characteristic low loss peaks of magnesium, at 10, 20 and 30 eV, have been measured [23-24].

Surrounding the MgH₂/Mg particles, a lighter contrast phase is present (Fig.6, region B). The comparison with a pure LiBH₄ sample gives the same texture and contrast as well as the same EDX spectra [18]. The EDX shows no signal from Mg atoms. In addition our EDX system is only able to detect elements with $Z=6$ (C) or above, meaning that neither Li nor B are detectable. Oxygen is however measurable as a consequence of expected partial oxidation of sensible samples due to residual vacuum gases in the microscope. The here presented electron diffraction image (Fig.6, region B) indicates however an amorphous phase, that does not correspond with the expected crystallinity of the LiBH₄ phase after XRD analysis. It is clear that the lighter contrast phase, surrounding the MgH₂/Mg particles, corresponds to LiBH₄ that undergoes decomposition by electron beam irradiation. The observed phases should correspond to amorphous products from the degradation (and/or oxidation) reactions of the material under observation inside the microscope. Other authors have also reported the difficulties to characterize by TEM techniques light borohydride compounds [25-26]. Boron, lithium and oxygen are therefore the main elements to be expected in the areas of lighter contrast. The EELS spectra at the B K-edge have been recorded and compared to data in reference compounds: LiBH₄, MgB₂, B and B₂O₃. By considering the spectra as a characteristic fingerprint, the degradation products of the LiBH₄ phase seem to be the same both in the sample and in the pure material and appear to be boron oxide like species. The MgB₂ phase, characterized by a clear resonance just before 190 eV, is not detected in this sample. The Li K-edge was not well detected due to the low cross section of this transition and overlapping with Mg L-edges and plasmon losses [27]. The oxygen K-edge is similar in all regions to the one reported in figure 6 for region B. In general it appears similar to the one measured in a pure LiBH₄ phase, indicating that

this phase is the most sensible to oxidation and degradation under our experimental conditions. The MgH_2/Mg phase appears more stable against oxidation.

Figure 7 corresponds to the study of $2\text{LiBH}_4+\text{MgH}_2+\text{Ti}$ -iso after ball milling. In a similar way to the one described for the sample without additive, darker and denser grains (region A') of 0.1-1 μm size correspond to the MgH_2/Mg phase. These large grains are polycrystalline and contain the MgH_2 nanocrystals determined by XRD. An amorphous phase (according to SAED data, not shown) is surrounding the Mg-based grains corresponding to the LiBH_4 phase after electron beam decomposition. The EDX analysis in both regions (A' and B') shows an uniform distribution of titanium in the sample within the size range of observation. This homogeneous distribution of Ti in the sample reduces the differences in contrast between the Mg-based and Li-B-based regions, as compared to the sample without additive. A difference is however detected in the O K-edge EELS spectra. For the sample with additive the main source of oxygen should be the added Ti-isopropoxide, instead of the oxidation of reactive species in the sample. The observed O K-edge spectra is therefore different, for both A' and B' regions, as compared to the one presented in figure 6 for region B.

After first desorption from the as milled sample ($2\text{LiBH}_4+\text{MgH}_2$ -des) a microstructural analysis is shown in figure 8. The sample shows a more homogeneous distribution of contrast between grains although the formation of some elongated crystal of darker contrast embedded in a lighter matrix could be clearly detected. As expected from XRD data these crystals correspond to the formation of the MgB_2 phase. In fact the B K-edge spectrum of this sample is presenting the characteristic resonance just before 190 eV for the magnesium boride. The SAED pattern also show characteristic peaks for MgB_2 compatible with the average crystallite size (73 nm) determined by XRD. The low loss region does not show the characteristics plasmon peaks for metallic Mg.

The lighter matrix should correspond, according to XRD data, to the LiH phase. Nevertheless this phase has been probed to be also very unstable under electron beam irradiation by direct observation of a reference sample inside the microscope. Characteristic electron diffraction pattern from LiH was not clearly observed in this sample. Oxygen K-edge peaks indicates that decomposition of Li-based phases inside the microscope could be coupled to oxidation.

In Figure 9 data are presented for the desorbed sample in the presence of the Ti-based additive. The MgB_2 and LiH crystals should be smaller according to XRD data. Again the LiH phase (lighter contrast) is difficult to analyze because is very sensible to

electron beam irradiation. The formation of holes in the sample upon longer observation indicates this decomposition. It is however possible to distinguish elongated crystals of darker contrast with a size in the same range as the average crystallite size determined by XRD (38 nm) for the MgB_2 phase. This phase is also well identified at the B K-edge EELS spectrum in Figure 9. The reported results are in agreement with the plate-like growth model of MgB_2 as proposed in reference [19]. EDX, low loss and O K-edge data are similar to the ones reported for the sample without Ti additive.

The results for sample $2\text{LiBH}_4+\text{MgH}_2$ after 1 cycle are shown in Figure 10. The sample went back to similar morphology as the one observed in the as milled material. The main difference is observed in the MgH_2 phase. Large grains are again present but with a strong dark contrast. In this case they correspond to single or large crystals (see SAED from region C) instead of having a nanocrystalline character as observed in the milled material. The low loss EELS spectrum in these grains is compatible with the MgH_2/Mg phase for a thick sample showing low electron transmission.

The region D in figure 10 shows again the expected features for the degraded LiBH_4 . The amorphous nature, as measured by electron diffraction, is again a confirmation of the degradation of the crystalline LiBH_4 by observation in the microscope. The B and O K-edges clearly demonstrated the disappearance of the MgB_2 and the formation of boron oxide like species under electron beam irradiation.

In Figure 11 data are presented for the 1 cycle sample in the presence of the Ti-based additive. Mg rich (C') and B rich (D') regions are identified as in the original milled sample. Large grains of MgH_2/Mg are again present with a strong dark contrast constituted by single or large crystals (see SAED from region C'). The Ti signal both in EDX and EELS spectra is very weak indicating the high dispersion of the formed TiB_2 phase (18,19).

Discussion

A detailed kinetic analysis, previously described in reference [19], revealed that the dehydrogenation of the LiBH_4 phase in the RHC material is well described by a model consisting in a random nucleation of the MgB_2 phase followed by the Johnson-Mehl-Avrami (JMA) growth mechanism. The growth is controlled by an interface reaction leading to a constant interface velocity, or by a diffusion-controlled growth mechanism with a decelerating interface velocity [19]. The formation of dispersed TiB_2 nanocrystals, from decomposition of the Ti-iso additive, has been also demonstrated in

a previous paper [18]. This dispersed boride phase is proposed to favour heterogeneous nucleation of MgB_2 , therefore improving the kinetic and strongly reducing the incubation period for the second desorption step as shown in figure 1.

Our XRD and TEM results strongly support the proposed mechanism [15-19] that considers the role of the additive during the growth of MgB_2 as nucleation agent. In fact the dispersed TiB_2 phase [18], formed from the reactive Ti-isopropoxide additive, has the same crystal structure as MgB_2 and therefore supplies coherent interfaces for the heterogeneous nucleation of the MgB_2 phase. The higher number of nucleation sites explains the decrease in the crystallite size for the MgB_2 and LiH phases in presence of the additive. Typical average crystallite sizes for the cubic LiH and hexagonal MgB_2 phases are a few hundreds and several tens of nm respectively. Reductions in crystallite size in the presence of additive by a factor of 50% were observed (see table I and figure 5).

The formation of LiH and MgB_2 upon desorption was observed to be a key factor for reversibility [11,12] at lower temperatures. Re-absorption process occurs in one single step, as observed in figure 1. Previous results in reference [19], comprising the analysis of the kinetics curves, revealed a contracting-volume controlled reaction for both MgB_2 decomposition and MgH_2 formation. This indicates that the MgB_2 phase is consumed from the surface to the centre and explains the single-step absorption reaction. Therefore it is proposed that the interface reaction during decomposition of MgB_2 is the rate-limiting step. The here observed (by XRD and TEM analysis) grain refinement effects of both MgB_2 and LiH phases are therefore important to improve the kinetics of the absorption reaction.

The reduction of crystallite size during the milling process of the LiBH_4 and MgH_2 phases is lost after the first cycle (see data in Table I and figure 5). Successive cycling of the materials produces a moderate grain refinement and the stabilization of the reaction kinetics. The improvement in kinetic may therefore be attributed to the high dispersion of the additive produced during the milling what is mandatory for an efficient heterogeneous nucleation during the dehydrogenation process.

Although the LiBH_4 phase is melting at operating temperatures, both desorption and absorption processes in the RHC system occur at liquid-solid interface due to the presence of solid Mg, LiH, and MgB_2 phases. The presented results in this paper show that microstructural effects, mainly related to the high dispersion of titanium borides at the grain boundaries, are the origin of kinetic improvements by favouring

heterogeneous nucleation reactions, grain refinement and increasing the number of heterogeneous reaction sites.

Grain refinement of MgB_2 due to enhanced nucleation frequency during several desorption processes is proposed, which results in kinetic improvements both in desorption and absorption. No experiments have been done to determine the number of cycles that the systems can overcome without deterioration of the kinetics. However, based on the proposed mechanism, a substantial decrease of reaction rates is not expected upon cycling if crystallite sizes are not increasing. According to the XRD data for crystallite sizes comparing 1 and 3 cycled samples, it is clear how up to three desorption cycles, as shown in Figure 1a, a reduction of H_2 desorption rate is not observed.

The data presented from transmission electron microscopy and spectroscopic analyses are in agreement with XRD results. It is also clear that differentiation should be done between grain and crystallite size what is especially important in the materials under investigation. Special care must be taken to analyse the TEM data for this kind of samples of high sensitivity to electron beam irradiation.

Conclusions

An exhaustive microstructural characterization is reported for the $\text{LiBH}_4\text{-MgH}_2$ RHC system with and without the Ti-isopropoxide additive. XRD data with Rietveld analysis and TEM studies coupled to EDX, SAED and EELS are presented here as the first time for this system in all sorption steps. Complementarities between XRD and TEM have been shown very useful for sensible samples that deteriorate under electron beam irradiation. Both lithium based phases (LiBH_4 and LiH) have been found to be very unstable (oxidation and decomposition) under electron beam irradiation; therefore only indirect conclusions were obtained from the TEM analysis.

No direct data were obtained in this study regarding the evolution of the Ti-based additive. Based on the previous studies in references [18] and [19], the formation at the grain boundaries of well dispersed TiB_2 (and titanium oxides) small additive nanoparticles, is the main factor improving desorption kinetics by favouring heterogeneous nucleation of MgB_2 . In this work it has been demonstrated that the higher number of nucleation sites in the presence of the additive is producing a decrease in the crystallite size for the MgB_2 and LiH phases during desorption. Reductions by a

factor of 50 % in crystallite size for these phases were measured in the presence of additive.

The reduction of crystallite size during the milling process of the LiBH_4 and MgH_2 phases is lost after the first cycle. Successive cycling of the materials produces a moderate grain refinement and the stabilization of the reaction kinetics. The main effects of the Ti-iso additive for kinetic improvement have been therefore identified as heterogeneous nucleation of MgB_2 in desorption, resulting in its grain refinement which improves kinetics in the subsequent absorption. High dispersion of the additive obtained during milling is mandatory for a fast sorption process.

Acknowledgements

Financial support by the Marie Curie Program (MRTN-CT-2006-035366), as well as the Spanish MICINN (CTQ2009-13440) and the Junta de Andalucía are acknowledged.

References

- [1] M. Fichtner. *Adv Eng Mater* 2005; 6:433.
- [2] L. Schlapbach, A. Züttel. *Nature* 2001; 414:353.
- [3] M. Dornheim, N. Eigen, G. Barkhordarian, T. Klassen, R. Bormann. *Adv Eng Mater* 2006; 8:377.
- [4] O. Friedrichs, A. Borgschulte, S. Kato, F. Buchter, R. Gremaud, A. Remhof, A. Züttel. *Chem Eur J* 2009; 15:5531.
- [5] A. Züttel, S. Renth, P. Fischer, P. Wenger, P. Sudan, Ph. Mauron, Ch. Emmenegger. *J Alloy Compd* 2003; 356-357:515.
- [6] J.J. Vajo, S.L. Skeith, F. Mertens. *Phys Chem B* 2005; 109:3719.
- [7] G. Barkhordarian, T. Klassen, M. Dornheim, R. Bormann. *J Alloy Compd* 2007; 440:L18
- [8] S. Orimo, Y. Nakamori, G. Kitahara, K. Miwa, N. Ohba, S. Towata, A. Züttel. *J Alloy Compd* 2005; 404-406:427
- [9] P. Mauron, F. Butcher, O. Friedrichs, A. Remhof, M. Biemann, C.N. Zwicky, A. Züttel. *J Phys Chem B* 2008; 112:906.
- [10] O. Friedrichs, F. Buchter, A. Borgschulte, A. Remhof, C.N. Zwicky, Ph. Mauron, M. Biemann, A. Züttel. *Acta Mater* 2008; 56:949.
- [11] U. Bösenberg, S. Doppiu, L. Mosegaard, G. Barkhordarian, N. Eigen, A. Borgschulte, T. Jensen, Y. Cerenius, O. Gutfleisch, T. Klassen, M. Dornheim, R. Bormann. *Acta Mater* 2007; 55:3951.
- [12] J.J. Vajo, T.T. Salguero, A.F. Gross, S.L. Skeith, G.L. Olson. *J Alloy Compd* 2007; 446-447:409.
- [13] M.-Q. Fan, L.-X. Sun, Y. Zhang, F. Xu, J. Zhang, H.-L. Chu. *Int J Hydrogen Energy* 2008; 33:74.
- [14] G. Barkhordarian, T. R. J., S. Doppiu, U. Bösenberg, A. Borgschulte, R. Gremaud, Y. Cerenius, M. Dornheim, T. Klassen, R. Bormann. *J Phys Chem C* 2008, 112:2743.
- [15] U. Bösenberg, U. Vainio, P.K. Pranzas, J.M. Bellosta von Colbe, G. Goerigk, E. Welter, M. Dornheim, A. Schreyer, R. Bormann. *Nanotech* 2009; 20:204003.
- [16] A.Yu. Ignatov, J. Graetz, S. Chaudhuri, T.T. Salguero, J.J. Vajo, M.S. Meyer, F.E. Pinkerton, T.A. Tyson. *X-Ray Absorption Fine Structure- XAFS 13*. In: 13th Int conference, Int XAFS Society, American Inst. of Physics 2007; 882:642.
- [17] J. Graetz, S. Chaudhuri, T.T. Salguero, J.J. Vajo, M.S. Meyer, F.E. Pinkerton, T.A. Tyson. *Nanotech* 2009; 20:204007.
- [18] E. Deprez, M.A. Muñoz-Márquez, M.A. Roldán, C. Prestipino, F.J. Palomares, C. Bonatto Minella, U. Bösenberg, M. Dornheim, R. Bormann, A. Fernández. *J Phys Chem C* 2010; 114:3309
- [19] U. Bösenberg, J.W. Kim, D. Gossler, N. Eigen, T.R. Jensen, J.M. Bellosta von Colbe, Y. Zhou, M. Dahms, D.H. Kim, R. Günther, Y.W. Cho, K.H. Oh, T. Klassen, R. Bormann, M. Dornheim. *Acta Mater* 2010; 58:3381.
- [20] L. Lutterotti, R. Ceccato, R. Dal Maschio, E. Pagani. *Mat. Sci. Forum* 1998; 278-281:87.
- [21] MAUD Materials Analysis Using Diffraction, www.ing.unitn.it/wmaud
- [22] O. Friedrichs, J.C. Sánchez-López, C. López-Cartés, M. Dornheim, T. Klassen, R. Bormann, A. Fernández. *Appl Surf Sci* 2006; 252:2334.
- [23] C.C. Ahn, O.L. Krivanek, *EELS Atlas*, Editor Gatan Inc.; 1983.
- [24] J.M. Thomas, T.G. Sparrow, M.K. Uppal, B.G. Williams. *Philosophical Transactions of the Royal Society A* 1986; 318:259
- [25] M. Fichtner, Z. Zhao-Karger, J. Hu, A. Roth, P. Weidler. *Nanotech* 2009; 20:204029.

- [26] B. Bogdanovic, M. Felderhoff, G. Streukens. *J Serb Chem Soc* 2009;74:183.
- [27] D. Blanchard, Q. Shi, C. B. Boothroyd, T. Vegge, *J Phys Chem C* 2009; 113:14059.

Figures captions

Fig. 1 – Desorption (a) and absorption (b) kinetic curves of $2\text{LiBH}_4+\text{MgH}_2$ and $2\text{LiBH}_4+\text{MgH}_2+5 \text{ mol } \% \text{ Ti-iso}$ (stars and circles respectively). In a) open circles for first desorption and grey filled circles for third desorption upon cycling. The oven temperature as a function of time is included (dash line), the temperature is reflected in the right axis.

Fig. 2 – XRD patterns of $2\text{LiBH}_4+\text{MgH}_2$ and $2\text{LiBH}_4+\text{MgH}_2+5 \text{ mol } \% \text{ Ti-iso}$ after ball milling (a) and after desorption (b). Peaks of references phases are indexed above: tetragonal MgH_2 ($\beta\text{-MgH}_2$), orthorhombic LiBH_4 , cubic MgO , hexagonal MgB_2 and cubic LiH . The hexagonal MgH_2 phase ($\gamma\text{-MgH}_2$) is indicated by symbols.

Fig. 3 – XRD patterns of $2\text{LiBH}_4+\text{MgH}_2$ and $2\text{LiBH}_4+\text{MgH}_2+5 \text{ mol } \% \text{ Ti-iso}$ after ball milling and after one cycle. Peaks of references phases are indexed above as in Fig. 2.

Fig. 4 – Experimental (circle) and fitted (line) X-ray diffraction patterns of $2\text{LiBH}_4+\text{MgH}_2+5 \text{ mol } \% \text{ Ti-iso}$ after ball milling. The difference pattern (between experimental and calculated data) and the diffraction patterns of fitted component phases (orthorhombic- LiBH_4 , $\beta\text{-MgH}_2$ and $\gamma\text{-MgH}_2$) are also shown.

Fig. 5 – Crystallites sizes (a) and microstrain (b) calculated by Rietveld method of as received materials (ar- LiBH_4 ; ar- MgH_2), pre-milled MgH_2 (pm- MgH_2), and materials after milling, desorption and absorption with or without Ti-iso. Numbers (1 to 5) are the same for both graph and explained on the right side up; filling of the bars, which are also the same for both graph, is explained on the right side down.

Fig. 6 – TEM micrograph for $2\text{LiBH}_4+\text{MgH}_2$ after ball milling, SAED and EDX spectra of A and B regions. Zero and low loss spectra in the A region, B and O K-edge spectra in the B region as compared to references (LiBH_4 , MgB_2 , B, B_2O_3 and MgH_2)

Fig. 7 - TEM micrograph for $2\text{LiBH}_4+\text{MgH}_2+5 \text{ mol } \% \text{ Ti-iso}$ after ball milling. SAED in region A', EDX spectra of A' and B' regions. Zero and low loss spectra in the A' region, B and O K-edge spectra in the B' and A' regions as compared to references (LiBH_4 , MgB_2 , B, B_2O_3 , MgH_2). Ti L-edge spectra in both B' and A' regions.

Fig. 8 - TEM micrograph for $2\text{LiBH}_4+\text{MgH}_2$ after desorption. SAED, EDX and low loss spectrum. B and O K-edge spectra compared to references (LiBH_4 , MgB_2 , B and LiH). The arrow indicates a MgB_2 crystal.

Fig. 9 – TEM micrograph for $2\text{LiBH}_4+\text{MgH}_2+5 \text{ mol } \% \text{ Ti-iso}$ after desorption. SAED, EDX and low loss spectrum. B and O K-edge spectra compared to references (LiBH_4 , MgB_2 , B and LiH). The arrow indicates a MgB_2 crystal.

Fig. 10 - TEM micrograph for $2\text{LiBH}_4+\text{MgH}_2$ after desorption and absorption. SAED in C and D regions. EDX spectrum in region C. Zero and low loss spectra in the C region. B and O K-edge spectra in the region D as compared to references (LiBH_4 , MgB_2 , B, B_2O_3 , MgH_2)

Fig. 11 - TEM micrograph for $2\text{LiBH}_4+\text{MgH}_2+5 \text{ mol } \% \text{ Ti-iso}$ after desorption and absorption. SAED, EDX, zero and low loss spectra in region C'. B and O K-edge spectra in the region D' as compared to references (LiBH_4 , MgB_2 , B, B_2O_3 , MgH_2).

Samples*	Majority phases	Refinement parameter R_{wp} (%)	Average crystallite sizes (nm)**	Average microstrain (%)**
2LiBH ₄ +MgH ₂	LiBH ₄ (ortho.)	16.2	265	0.000755
	β-MgH ₂ (tetra.)		12.5	0.0014
	γ-MgH ₂ (hexa.)		25	0.015
2LiBH ₄ +MgH ₂ +des	LiH (cubic)	17	261	0.00088
	MgB ₂ (hexa.)		73	0.0015
2LiBH ₄ +MgH ₂ +1 cycle	LiBH ₄ (ortho.)	21	520	0.00079
	β-MgH ₂ (tetra.)		1100	0.000967
2LiBH ₄ +MgH ₂ +5Ti-iso	LiBH ₄ (ortho.)	12	420	0.0021
	β-MgH ₂ (tetra.)		16	0.002
	γ-MgH ₂ (hexa.)		20	0.0015
2LiBH ₄ +MgH ₂ +5Ti-iso+des	LiH (cubic)	15	116.5	0.00055
	MgB ₂ (hexa.)		38	0.0014
	MgO (cubic)		8.5	0.003
2LiBH ₄ +MgH ₂ +5Ti-iso+1 cycle	LiBH ₄ (ortho.)	20	410	0.0025
	β-MgH ₂ (tetra.)		1000	0.00087
	MgO (cubic)		99	0.016
2LiBH ₄ +MgH ₂ +5Ti-iso+3 cycles	LiBH ₄ (ortho.)	19	220	0.0012
	β-MgH ₂ (tetra.)		760	0.00086
	MgO (cubic)		10	0.0017
ar-LiBH ₄	LiBH ₄ (ortho.)	22	2120	0.00052
ar-MgH ₂	β-MgH ₂ (tetra.)	29	840	0.00082
pm-MgH ₂	β-MgH ₂ (tetra.)	20	12.5	0.0018

*As received materials: ar-LiBH₄ and ar-MgH₂

Pre-milled MgH₂: pm-MgH₂

Milling of pm-MgH₂ and LiBH₄ with/without additive: 2LiBH₄+MgH₂ and

2LiBH₄+MgH₂+Ti-iso

First desorption samples: 2LiBH₄+MgH₂+des and 2LiBH₄+MgH₂+Ti-iso+des

One cycle samples: 2LiBH₄+MgH₂+1 cycle and 2LiBH₄+MgH₂+Ti-iso+1 cycle

Three cycles sample: 2LiBH₄+MgH₂+Ti-iso+3 cycles

**Errors are 10% for crystallite sizes and microstrain values

Table 1: Crystallite sizes and microstrain obtained from Rietveld refinement of as received materials (ar-LiBH₄; ar-MgH₂), pre-milled MgH₂ (pm-MgH₂), and materials after milling, desorption and absorption with or without Ti-iso. The refinement parameter R_{wp} is also included.

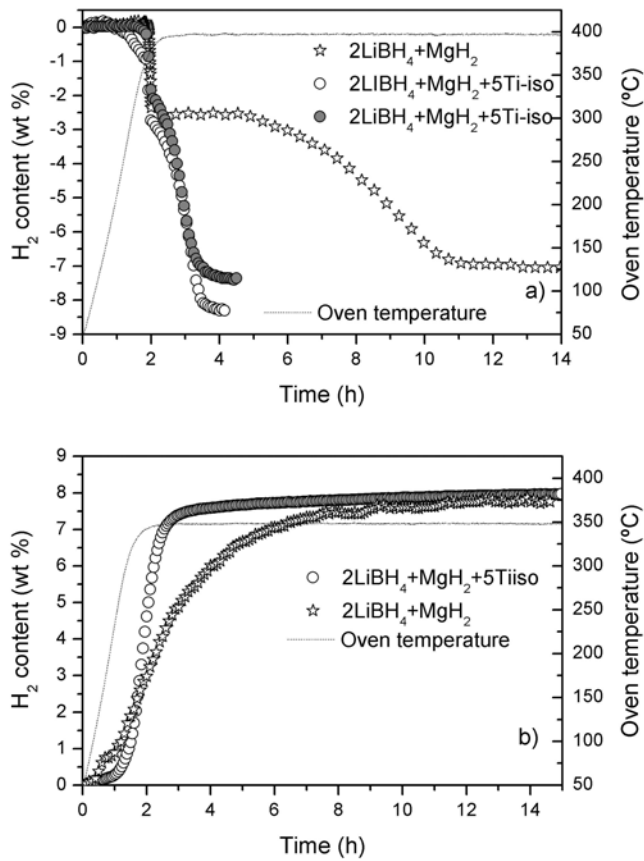


Fig. 1 – Desorption (a) and absorption (b) kinetic curves of $2\text{LiBH}_4+\text{MgH}_2$ and $2\text{LiBH}_4+\text{MgH}_2+5$ mol % Ti-iso (stars and circles respectively). In a) open circles for first desorption and grey filled circles for third desorption upon cycling. The oven temperature as a function of time is included (dash line), the temperature is reflected in the right axis.

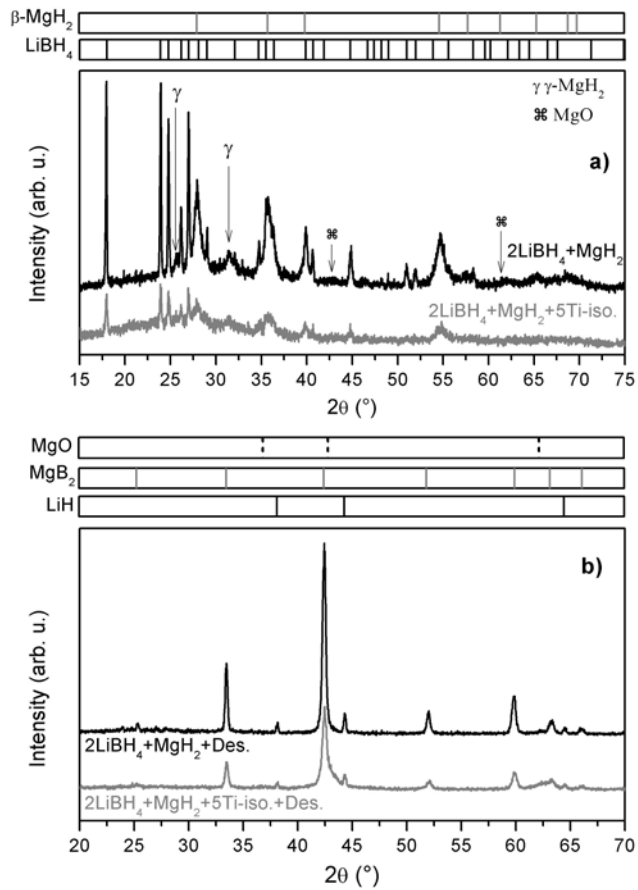


Fig. 2 – XRD patterns of $2\text{LiBH}_4 + \text{MgH}_2$ and $2\text{LiBH}_4 + \text{MgH}_2 + 5\text{ mol \% Ti-iso}$ after ball milling (a) and after desorption (b). Peaks of reference phases are indexed above: tetragonal MgH_2 ($\beta\text{-MgH}_2$), orthorhombic LiBH_4 , cubic MgO , hexagonal MgB_2 and cubic LiH . The hexagonal MgH_2 phase ($\gamma\text{-MgH}_2$) is indicated by symbols.

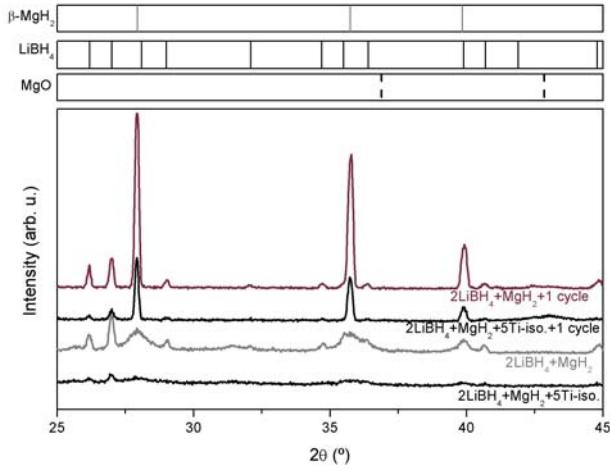


Fig. 3 – XRD patterns of $2\text{LiBH}_4+\text{MgH}_2$ and $2\text{LiBH}_4+\text{MgH}_2+5$ mol % Ti-iso after ball milling and after one cycle. Peaks of references phases are indexed above as in Fig. 2.

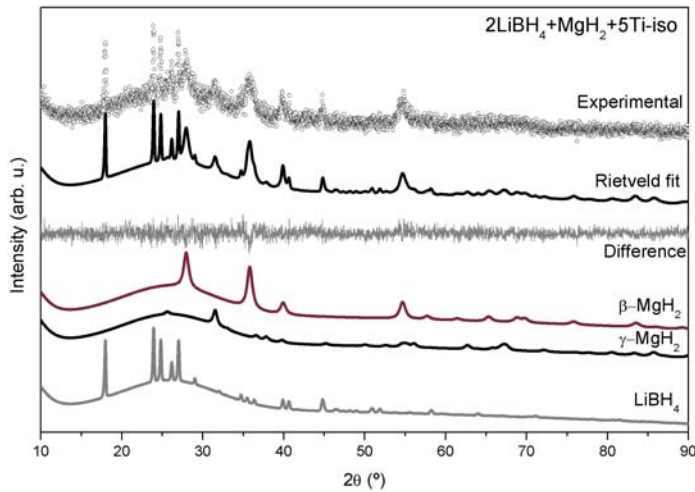


Fig. 4 – Experimental (circle) and fitted (line) X-ray diffraction patterns of $2\text{LiBH}_4+\text{MgH}_2+5$ mol% Ti-iso after ball milling. The difference pattern (between experimental and calculated data) and the diffraction patterns of fitted component phases (orthorhombic- LiBH_4 , $\beta\text{-MgH}_2$ and $\gamma\text{-MgH}_2$) are also shown.

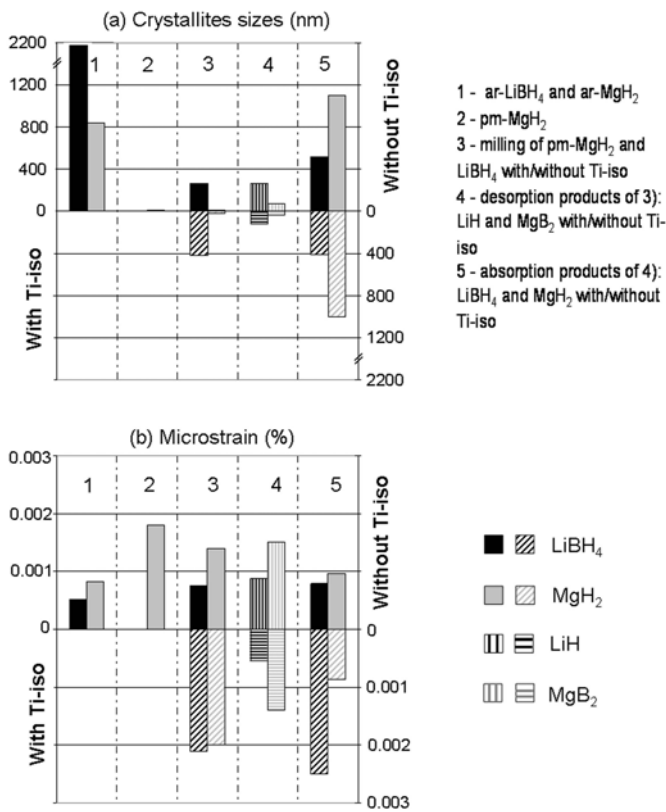


Fig. 5 – Crystallites sizes (a) and microstrain (b) calculated by Rietveld method of as received materials (ar-LiBH₄; ar-MgH₂), pre-milled MgH₂ (pm-MgH₂), and materials after milling, desorption and absorption with or without Ti-iso. Numbers (1 to 5) are the same for both graph and explained on the right side up; filling of the bars, which are also the same for both graph, is explained on the right side down.

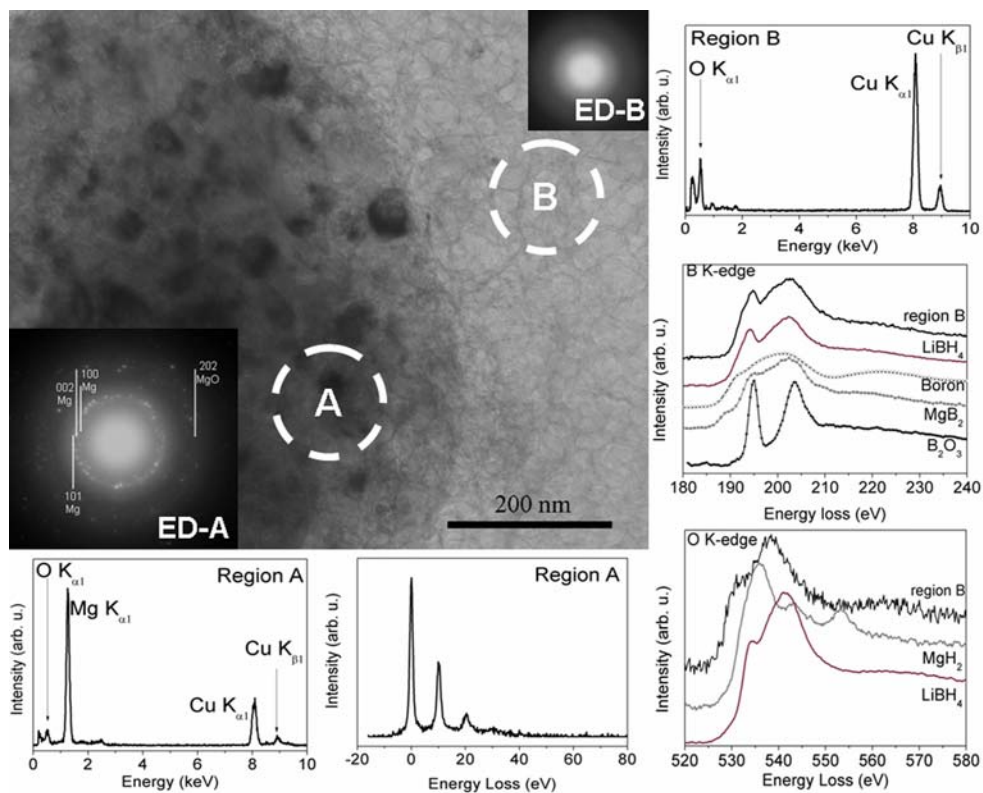


Fig. 6 – TEM micrograph for $2\text{LiBH}_4 + \text{MgH}_2$ after ball milling, SAED and EDX spectra of A and B regions. Zero and low loss spectra in the A region, B and O K-edge spectra in the B region as compared to references (LiBH_4 , MgB_2 , B, B_2O_3 and MgH_2)

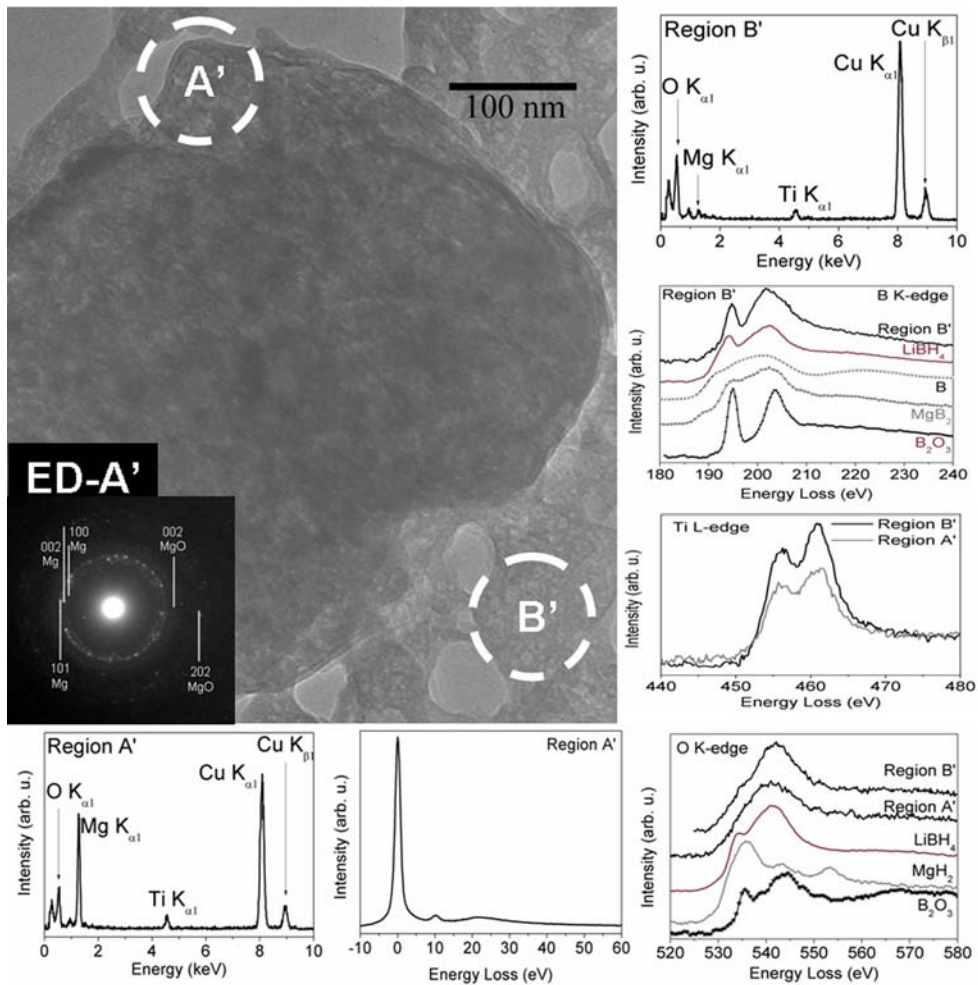


Fig. 7 - TEM micrograph for $2\text{LiBH}_4 + \text{MgH}_2 + 5 \text{ mol } \% \text{ Ti-iso}$ after ball milling. SAED in region A', EDX spectra of A' and B' regions. Zero and low loss spectra in the A' region, B and O K-edge spectra in the B' and A' regions as compared to references (LiBH_4 , MgB_2 , B, B_2O_3 , MgH_2). Ti L-edge spectra in both B' and A' regions.

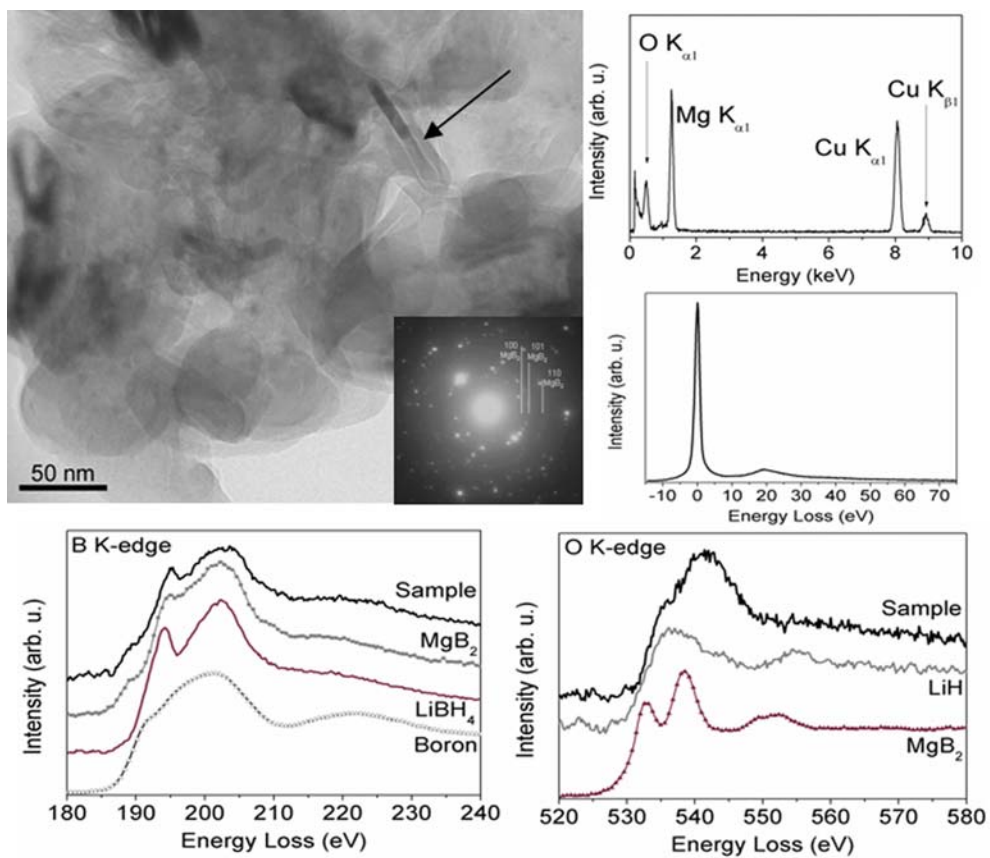


Fig. 8 - TEM micrograph for $2\text{LiBH}_4 + \text{MgH}_2$ after desorption. SAED, EDX and low loss spectrum. B and O K-edge spectra compared to references (LiBH_4 , MgB_2 , B and LiH). The arrow indicates a MgB_2 crystal.

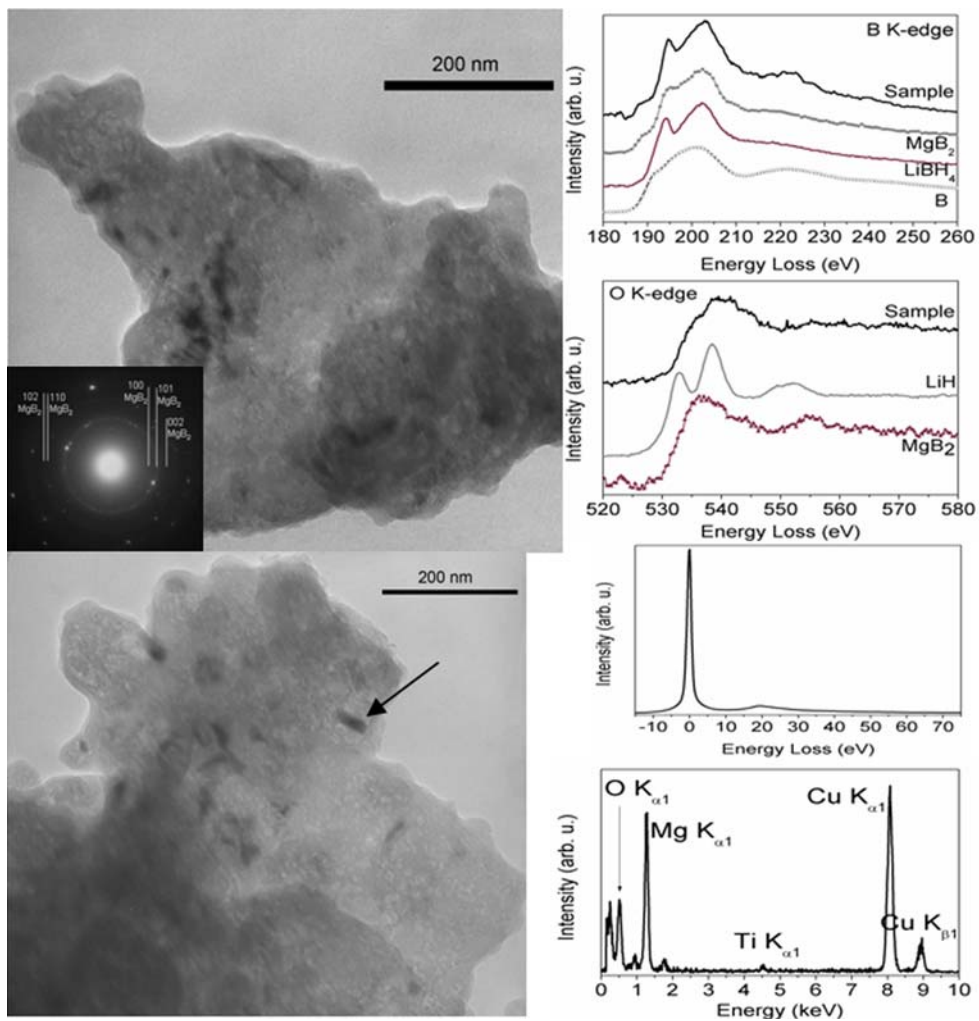


Fig. 9 – TEM micrograph for 2LiBH₄+MgH₂+5 mol % Ti-iso after desorption. SAED, EDX and low loss spectrum. B and O K-edge spectra compared to references (LiBH₄, MgB₂, B and LiH). The arrow indicates a MgB₂ crystal.

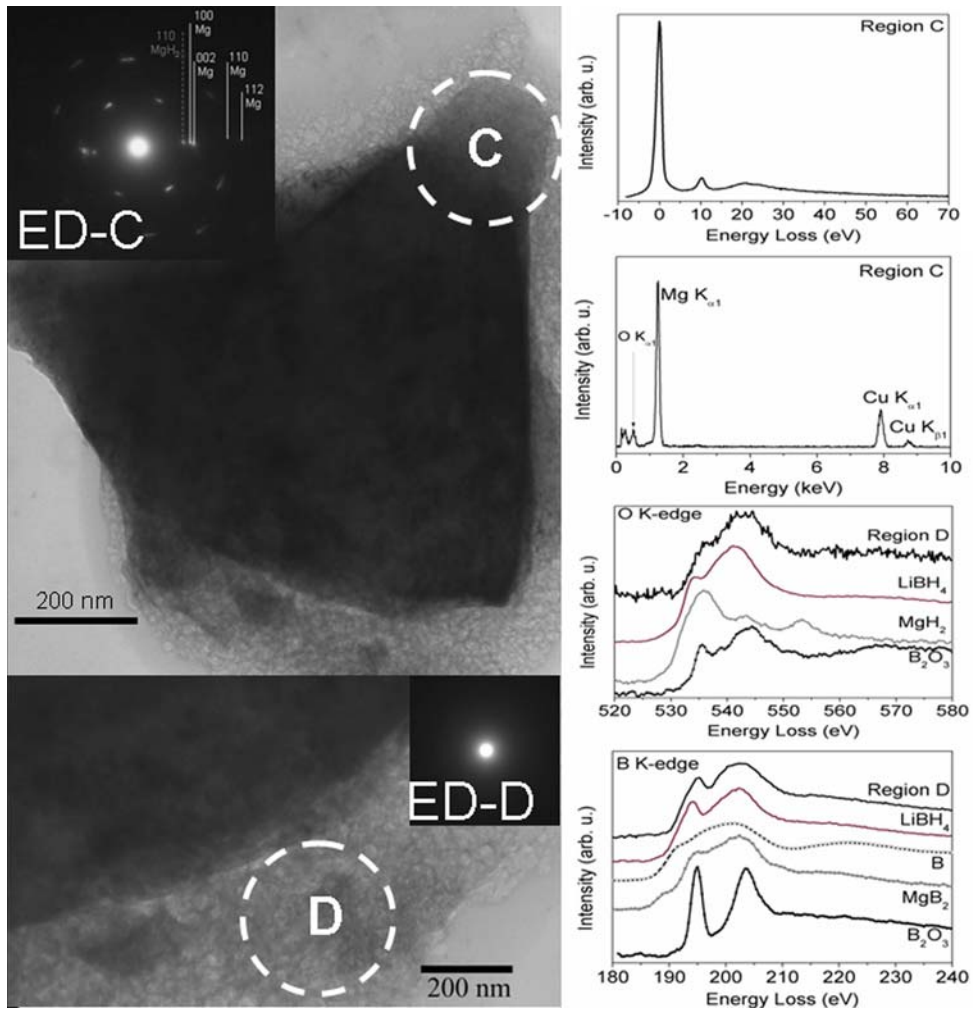


Fig. 10 - TEM micrograph for $2\text{LiBH}_4 + \text{MgH}_2$ after desorption and absorption. SAED in C and D regions. EDX spectrum in region C. Zero and low loss spectra in the C region. B and O K-edge spectra in the region D as compared to references (LiBH_4 , MgB_2 , B, B_2O_3 , MgH_2)

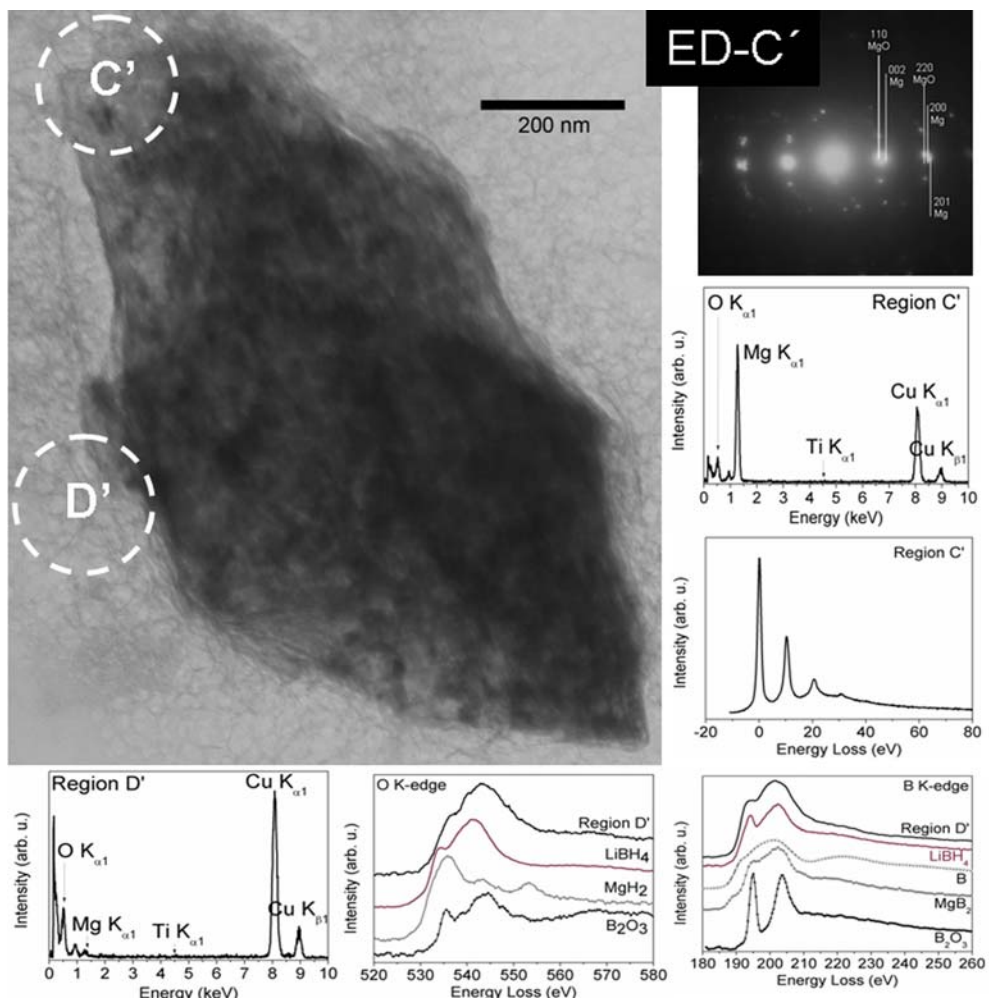


Fig. 11 - TEM micrograph for 2LiBH₄+MgH₂+5 mol % Ti-iso after desorption and absorption. SAED, EDX, zero and low loss spectra in region C'. B and O K-edge spectra in the region D' as compared to references (LiBH₄, MgB₂, B, B₂O₃, MgH₂).